Off-axis holographic tomography for diffracting scalar wavefields

Daxin Shi and Mark A. Anastasio*
Department of Biomedical Engineering, Illinois Institute of Technology, Chicago, Illinois 60616, USA
(Received 23 August 2005; published 23 January 2006)

Inverse scattering theories are available that permit tomographic reconstruction of the complex-valued refractive index distribution of weakly scattering objects from knowledge of intensity measurements. These imaging methods are valuable in applications that involve high-frequency optical wavefields, in which direct wavefield phase measurements can be difficult experimentally. The so-called in-line holographic imaging geometry has been well-studied, in which two measurements of the forward scattered wavefield intensity are acquired on distinct parallel detector planes that are perpendicular to the direction of the illuminating wavefields. In this work, based on the principles of intensity diffraction tomography, a reconstruction theory for *off-axis* holographic tomography with diffracting scalar wavefields is developed and investigated. A distinct feature of the method is that, at each tomographic view angle, the object is illuminated by use of two plane waves that propagate in different directions. The intensities of the forward scattered wavefields are measured on a *single* detector behind the object. This permits the direction of the probing wavefield to be varied for acquisition of the necessary measurement data, rather than the detector placement as required by conventional in-line holographic methods. The developed image reconstruction method is validated and investigated by use of computer-simulation studies.

DOI: 10.1103/PhysRevE.73.016612 PACS number(s): 42.30.Wb, 42.25.Fx, 42.30.Va, 42.30.Rx

I. INTRODUCTION

Diffraction tomography [1–3] (DT) is a linearized inverse scattering technique for determination of the three-dimensional (3D) complex-valued refractive index distribution of weakly scattering objects. The physics embodied by DT reconstruction theory is relevant to a wide range of imaging problems that can be described mathematically by a scalar Helmholtz equation. Applications of DT imaging arise, for example, in optics [4–6], coherent x-ray imaging [7], geophysics [8], and acoustics [9,10]. In conventional DT methods, an object is illuminated by a time-harmonic scalar diffracting wavefield, and the amplitude and phase of the forward scattered wavefield are measured on a plane behind the object. In high-frequency applications, such as arise in optics or coherent x-ray imaging, this aspect of DT is undesirable because the wavefield phase can be difficult to measure experimentally [4,11,12].

To circumvent the need to measure wavefield phase information, intensity-based DT reconstruction methods have been developed [5,13–17] that utilize in-line holographic measurement geometries. One such method, which we have termed [18,19] *intensity DT* (I-DT), has been proposed in recent years by Gbur and Wolf [15,16]. Intensity DT circumvents the need to measure the forward scattered wavefield phase by requiring two or more measurements of wavefield intensity in different parallel detector planes that are perpendicular to the direction of the probing wavefield. Each of these intensity measurement represents an in-line Gabor hologram [20], in which information regarding the wavefield phase is encoded as variations in the recorded intensity. From knowledge of these intensity measurements acquired at a collection of tomographic view angles, an estimate of the object's 3D complex-valued refractive index distribution can be reconstructed. As with conventional DT, I-DT requires that the object be weakly scattering in the sense that the first-order Rytov approximation is valid [21].

It should be noted that I-DT differs from classic sideband holographic imaging methods [11,22] in two important respects. First, the I-DT method does not involve the use of a reference beam to illuminate the recorded hologram. Both intensity measurements in I-DT correspond to wavefields that illuminate the object. Second, I-DT permits direct reconstruction of the refractive index distribution without an explicit intermediate step of recovering the wavefield phase. In essence, the I-DT method recovers the required phase information implicitly during the tomographic reconstruction process.

In this paper, a reconstruction theory for *off-axis* holographic tomography with diffracting scalar wavefields is developed and investigated. By *off-axis* holographic tomography, we refer to a generalized in-line I-DT method in which two intensity measurements are acquired on a single fixed detector plane behind the object. The first of these measurements corresponds to an illuminating plane wave propagating in a direction perpendicular to the detector plane; this measurement is the same as would be acquired in a conventional in-line geometry. The second measurement, however, is not a conventional in-line measurement and corresponds to an illuminating plane wave propagating obliquely with respect to this direction. Accordingly, in off-axis holographic tomography, the direction of the incident plane wave represents the degree of freedom that is varied for acquisition of the measurement data rather than the detector location as in conventional in-line methods. By use of tomographic symmetries, we demonstrate mathematically that the intensity measurements acquired in this geometry uniquely determine

*Corresponding author. Fax: (312)567-5707. Email address: anastasio@iit.edu

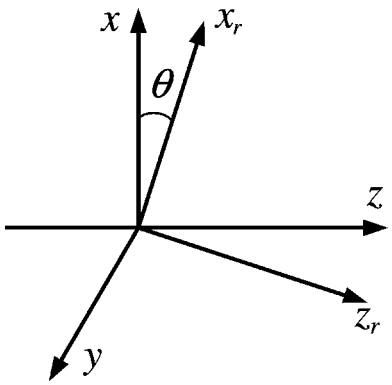

FIG. 1. The rotated coordinate system used to describe the tomographic measurement geometry.

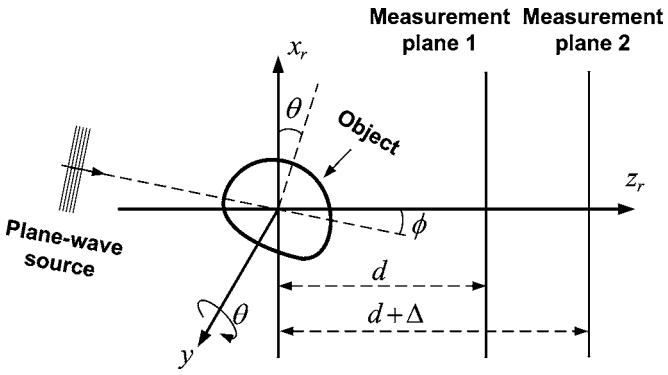

FIG. 2. In I-DT, a plane wave with incidence angle $\phi_{in}=\phi$ irradiates the object and the intensity of the forward scattered wavefield is measured on two detector planes $z_r=d$ and $z_r=d+\Delta$, respectively. Tomographic scanning is achieved by simultaneously rotating the source and detector plane about the y axis.

Fourier components of the scattering potential that are conveyed by propagating wave modes. Our analysis reveals that, in the presence of data noise or other data inconsistencies, certain spatial frequency components cannot be determined accurately due to the effects of singularities in the reconstruction formula. A reconstruction algorithm is derived for obtaining an estimate of the scattering potential from its determined Fourier components. A preliminary numerical investigation of the reconstruction algorithm is presented to demonstrate its use and corroborate our theoretical assertions.

The article is organized as follows. In Sec. II, we review the salient features of conventional I-DT reconstruction theory that provide a basis for our analysis. In Sec. III, Fourier space data symmetries are identified and utilized for the development of a reconstruction formula for off-axis holographic tomography. The computer-simulation study is presented in Sec. IV, and a discussion and summary of the work is provided in Sec. V.

II. BACKGROUND

In this section, we survey some results from conventional I-DT reconstruction theory [15,16] that are necessary for the development of our imaging theory. To facilitate the description of the tomographic scanning geometry, we will utilize a rotated coordinate system $\vec{r}=(x_r,y,z_r)$ that is shown in Fig. 1. The rotated system is related to the reference system $\vec{r}=(x,y,z)$ by $x_r=x\cos\theta+z\sin\theta$ and $z_r=-x\sin\theta+z\cos\theta$, where the angle θ is measured from the positive x axis. As described below, θ will denote the tomographic view angle. The unit vectors $\hat{s}_{1,r}$, $\hat{s}_2$, and $\hat{s}_{0,r}$ indicate the positive x_r, y, and z_r axes, respectively. If needed, the θ dependence of $\hat{s}_{1,r}$ and $\hat{s}_{0,r}$ will be denoted as $\hat{s}_{1,r}(\theta)$ and $\hat{s}_{0,r}(\theta)$, respectively.

A. Review of plane-wave I-DT

Consider the I-DT scanning geometry illustrated in Fig. 2. A monochromatic scalar plane wave

$$U_{in}(\vec{r})=\exp(i\vec{k}\cdot\vec{r}) \tag{1}$$

is incident on a weakly scattering object that occupies volume V. Here, $i\equiv\sqrt{-1}$, $\vec{k}$ is the wave vector with magnitude k, and a harmonic time-dependence $\exp(-i\omega t)$ is assumed. In the rotated coordinate system, $\vec{k}$ is expressed as $\vec{k}=(k\sin\phi_{in},0,k\cos\phi_{in})$ where, as shown in Fig. 2, ϕ_{in} is measured from the positive z_r axis. Two measurements of the transmitted wavefield intensity are recorded on the detector planes $z_r=d$ and $z_r=d+\Delta$, where $\Delta>0$. I-DT employing a conventional in-line geometry [15,16] corresponds to the special case where $\vec{k}=k\hat{s}_{0,r}$, i.e., $\phi_{in}=0$, and the detector planes are perpendicular to the direction of the illuminating plane wave. Tomographic scanning is accomplished by simultaneously rotating the incident plane-wave source and detector planes by an angle $\theta\in[0,2\pi)$ about the y axis. As reviewed in Sec. II B, the resulting intensity measurements permit reconstruction of an estimate of the scattering potential $f(\vec{r})$ that is defined by the object's complex-valued refractive index distribution $n(\vec{r})$ as

$$f(\vec{r})\equiv\frac{k^2}{4\pi}[n^2(\vec{r})-1]. \tag{2}$$

It is physically reasonable to assume that $f(\vec{r})$ is a bounded function with compact support. The equations that relate $f(\vec{r})$ to the measured intensity data in I-DT are presented below.

Behind the object, the transmitted wavefield can be expressed as

$$U(\vec{r})=U_{in}(\vec{r})\exp[\psi(\vec{r})], \tag{3}$$

where $\psi(\vec{r})$ is a complex phase function. Assuming that the interaction of $U_{in}(\vec{r})$ with the object is described by coherent scattering that is sufficiently weak [23], $\psi(\vec{r})$ can be related to the scattering potential $f(\vec{r})$ via the first-Rytov approximation (e.g., see Ref. [21], chap. 13) as

$$\psi(\vec{r})=\frac{1}{U_{in}(\vec{r})}\int_V f(\vec{r}')\frac{\exp[jk|\vec{r}-\vec{r}'|]}{|\vec{r}-\vec{r}'|}U_{in}(\vec{r}')\,d\vec{r}'. \tag{4}$$

Let $\psi(x_r,y,\theta;\phi_{in},z_r)$ denote $\psi(\vec{r})$ evaluated on a plane of constant z_r at tomographic view angle θ, corresponding to an incident plane wave with orientation ϕ_{in}. The functions

$$\hat{\psi}(u_r,v,\theta;\phi_{in},z_r)=\frac{1}{(2\pi)^2}\int\int_{\mathbb{R}^2}\psi(x_r,y,\theta;\phi_{in},z_r)\times\exp[-i(u_rx_r+vy)]\,dx_rdy \tag{5}$$

and

$$\hat{F}(\vec{K})=\frac{1}{(2\pi)^3}\int_{\mathbb{R}^3}f(\vec{r})\exp[-i\vec{K}\cdot\vec{r}]\,d\vec{r} \tag{6}$$

will denote the two-dimensional (2D) and 3D Fourier transform of $\psi(x_r,y,\theta;\phi_{in},z_r)$ and $f(\vec{r})$, respectively. Note that the frequency variables u_r and v are the Fourier conjugates to the detector plane coordinates x_r and y, respectively. The vector $\vec{K}=(u_r,v,\nu_z)$ is the Fourier conjugate to $\vec{r}=(x_r,y,z_r)$ and describes a point in 3D Fourier space by use of a rotated coordinate system.

Under these conditions, the generalized Fourier diffraction projection (FDP) theorem indicates that [8]

$$\hat{\psi}(u_r,v,\theta;\phi_{in},z_r)=\frac{i(2\pi)^2e^{iz_r[\sqrt{k^2-(u_r+k\sin\phi_{in})^2-v^2}-k\cos\phi_{in}]}}{\sqrt{k^2-(u_r+k\sin\phi_{in})^2-v^2}}\times\hat{F}[u_r,v,\omega(u_r,v,\phi_{in});\theta], \tag{7}$$

where

$$\hat{F}[u_r,v,\omega(u_r,v,\phi_{in});\theta]\equiv\hat{F}(u_r\hat{s}_{1,r}(\theta)+v\hat{s}_2+\omega(u_r,v,\phi_{in})\hat{s}_{0,r}(\theta)), \tag{8}$$

and

$$\omega(u_r,v,\phi_{in})=\sqrt{k^2-(u_r+k\sin\phi_{in})^2-v^2}-k\cos\phi_{in}. \tag{9}$$

For $(u_r+k\sin\phi_{in})^2+v^2\leq k^2$, the points $(\nu_x,\nu_y,\nu_z)=(u_r,v,\omega(u_r,v,\phi_{in}))$ define the surface of a hemisphere (Ewald sphere) of radius k in Fourier space. Therefore, Eq. (7) indicates that the 2D Fourier transform of the complex phase function is linearly proportional to the 3D Fourier transform of the scattering potential evaluated on a hemisphere of radius k that is centered at $(-k\sin\phi_{in},0,-k\cos\phi_{in})$ in the rotated coordinate system. This relationship provides the basis for image reconstruction in DT [2,3].

In I-DT, only the wavefield intensity $I(x_r,y,\theta;\phi_{in},z_r)\equiv|U(\vec{r})|^2$ of the transmitted wavefield is assumed to be measurable on a detector plane of constant z_r. In this case, Eqn. (7) cannot be employed directly for image reconstruction because the complex phase $\psi(\vec{r})$ remains unknown. Consider the intensity data function

$$D_I(x_r,y,\theta;\phi_{in},z_r)\equiv\log I(x_r,y,\theta;\phi_{in},z_r), \tag{10}$$

whose 2D Fourier transform in the plane of constant z_r is denoted by $\hat{D}_I(u_r,v,\theta;\phi_{in},z_r)$. It can be shown readily (for the $\phi_{in}=0$ case, see Refs. [15,16]) that

$$\hat{D}_I(u_r,v,\theta;\phi_{in},z_r)=a^+(u_r,v;\phi_{in},z_r)\hat{F}[u_r,v,\omega(u_r,v,\phi_{in});\theta]+a^-(u_r,v;\phi_{in},z_r)\hat{F}^*[-u_r,-v,\omega(-u_r,-v,\phi_{in});\theta], \tag{11}$$

where * denotes the conjugate of a complex-valued quantity,

$$a^+(u_r,v;\phi_{in},z_r)=\frac{i(2\pi)^2e^{iz_r[\sqrt{k^2-(u_r+k\sin\phi_{in})^2-v^2}-k\cos\phi_{in}]}}{\sqrt{k^2-(u_r+k\sin\phi_{in})^2-v^2}}, \tag{12}$$

and

$$a^-(u_r,v;\phi_{in},z_r)=\frac{-i(2\pi)^2e^{-iz_r[\sqrt{k^2-(u_r-k\sin\phi_{in})^2-v^2}-k\cos\phi_{in}]}}{\sqrt{k^2-(u_r-k\sin\phi_{in})^2-v^2}}. \tag{13}$$

Throughout this paper, it will be assumed that the spatial frequencies u_r and v satisfy

$$k^2>(u_r\pm k\sin\phi_{in})^2+v^2. \tag{14}$$

The conditions in Eqs. (14) ensure that $\omega(u_r,v,\phi_{in})$ and $\omega(-u_r,-v,\phi_{in})$ are real valued, respectively, and therefore the Fourier components $\hat{F}[\cdots]$ and $\hat{F}^*[\cdots]$ in Eq. (11) correspond to real-valued spatial frequencies. Physically, this reflects that we do not attempt to utilize information carried by evanescent wave modes [6], which in this paper is assumed to be unavailable.

We will refer to Eq. (11) as the intensity Fourier diffraction projection (I-FDP) theorem. The I-FDP theorem relates the 2D Fourier transform of the intensity data function to a linear combination of two Fourier components of $f(\vec{r})$ that reside on the offset Ewald hemisphere in planes of constant $\pm v$, respectively. Because it is described by a single equation involving two unknowns, the I-FDP theorem demonstrates why, in general, Fourier components of $f(\mathbf{r})$ cannot be reconstructed from knowledge of $D_I(x_r,y,\theta;\phi_{in},z_r)$ acquired on a single detector plane for a fixed illuminating angle ϕ_{in}.

B. Image reconstruction using multiple detector planes

Conventional I-DT methods circumvent the difficulty mentioned above by keeping the illuminating angle ϕ_{in} fixed but acquiring an additional intensity measurement on a second detector plane at each tomographic view angle. According to Eq. (11), an intensity measurement acquired on a second detector plane $z_r=d+\Delta$, $\Delta>0$, satisfies

$$\hat{D}_I(u_r,v,\theta;\phi_{in},z_r+\Delta)=a^+(u_r,v;\phi_{in},z_r+\Delta)\hat{F}[u_r,v,\omega(u_r,v,\phi_{in});\theta]+a^-(u_r,v;\phi_{in},z_r+\Delta)\hat{F}^*[-u_r,-v,\omega(-u_r,-v,\phi_{in});\theta]. \tag{15}$$

Equations (11) and (15) represent a system of two equations with two unknowns whose solution yields [24]

$$\hat{F}[u_r,v,\omega(u_r,v,\phi_{in});\theta]=\frac{1}{M_2}\begin{vmatrix}\hat{D}_I(u_r,v,\theta;\phi_{in},z_r) & a^-(u_r,v;\phi_{in},z_r)\\ \hat{D}_I(u_r,v,\theta;\phi_{in},z_r+\Delta) & a^-(u_r,v;\phi_{in},z_r+\Delta)\end{vmatrix}, \tag{16}$$

where

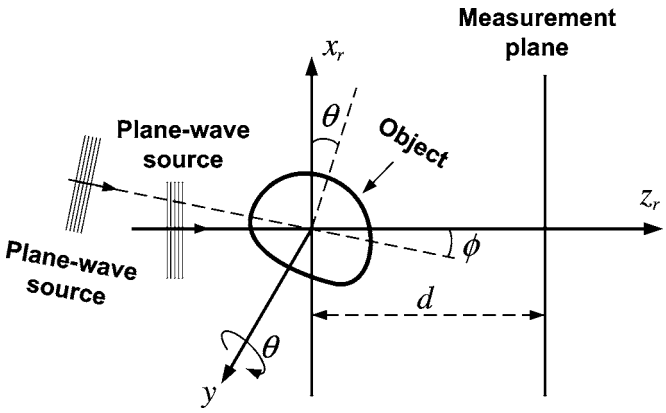

FIG. 3. In the off-axis measurement geometry, a plane wave with incidence angle $\phi_{in}=0$ irradiates the object and the intensity of the forward scattered wavefield is measured on the plane $z_r=d$. The measurement is repeated using a plane wave with incidence angle $\phi_{in}=\phi$, where $\phi\neq 0$. Tomographic scanning is achieved by simultaneously rotating the source and the detector plane about the y axis.

$$M_2 = \begin{vmatrix} a^+(u_r,v;\phi_{in},z_r) & a^-(u_r,v;\phi_{in},z_r) \\ a^+(u_r,v;\phi_{in},z_r+\Delta) & a^-(u_r,v;\phi_{in},z_r+\Delta) \end{vmatrix}. \tag{17}$$

When $\phi_{in}=0$, Eq. (16) reduces to the conventional plane-wave I-DT reconstruction formula in Refs. [15,16]. From the determined Fourier components $\hat{F}[u_r,v,\omega(u_r,v,\phi_{in});\theta]$, a low-pass filtered estimate of the 3D scattering potential $f(\vec{r})$ can be reconstructed by use of well-studied DT reconstruction algorithms [8,25,26].

III. OFF-AXIS HOLOGRAPHIC TOMOGRAPHY

In this section, the principles of I-DT are utilized for the development of a reconstruction theory for *off-axis* holographic tomography with diffracting scalar wavefields. The developed imaging method differs from I-DT in that it does not employ a conventional in-line measurement geometry. The direction of the incident plane wave represents the degree of freedom that is exploited for acquisition of the measurement data rather than the detector location as in traditional in-line methods.

A. Off-axis scanning geometry and data functions

Consider the scanning geometry illustrated in Fig. 3. At each tomographic view angle θ, two measurements of the transmitted wavefield intensity are recorded on the detector plane $z_r=d$. The first of these measurements will correspond to illumination angle $\phi_{in}^{(1)}=0$, i.e., an illuminating plane wave propagating in a direction that is perpendicular to the detector plane $z_r=d$. This measurement is the same as would be acquired on the first detector plane in an in-line geometry. The second measurement corresponds to an illuminating plane wave propagating obliquely with respect to this direction. This illumination angle is denoted by $\phi_{in}^{(2)}$ and satisfies $\phi_{in}^{(2)}\neq 0$ and $\phi_{in}^{(2)}\in(-\pi/2,\pi/2)$.We refer to such a measurement geometry as an *off-axis* holographic geometry. The key feature of this geometry is that the location of the detector plane is fixed and the illuminating angle ϕ_{in} of the incident plane wave represents the degree of freedom that is varied for acquisition of the measurement data. Tomographic scanning is accomplished by simultaneously rotating the incident wavefield sources and detector plane through an angle $\theta\in[0,2\pi)$ about the y axis. This measurement geometry is not accommodated by existing I-DT reconstruction methods, but may prove useful in certain practical imaging applications [5,27]. In the remainder of this paper, we develop a novel theory for image reconstruction in off-axis holographic tomography.

Because the location of the detector plane will remain fixed at $z_r=d$, the z_r dependence of the equations presented in Sec. II will be suppressed hereafter. According to Eq. (11), the measurements acquired by use of illuminating angles $\phi_{in}^{(1)}=0$ and $\phi_{in}^{(2)}=\phi$ are related to the scattering potential as

$$\hat{D}_I(u_r,v,\theta;\phi_{in}^{(1)}=0) = a^+(u_r,v;0)\hat{F}[u_r,v,\omega(u_r,v,0);\theta] + a^-(u_r,v;0)\hat{F}^*[-u_r,-v,\omega(-u_r,-v,0);\theta], \tag{18}$$

and

$$\hat{D}_I(u_r,v,\theta;\phi_{in}^{(2)}=\phi) = a^+(u_r,v;\phi)\hat{F}[u_r,v,\omega(u_r,v,\phi);\theta] + a^-(u_r,v;\phi)\hat{F}^*[-u_r,-v,\omega(-u_r,-v,\phi);\theta], \tag{19}$$

where the spatial frequencies u_r and v satisfy the conditions given in Eq. (14). Notice that these equations involve distinct Fourier components of $f(\vec{r})$. Accordingly, Eqs. (18) and (19) represent a system of two equations with four unknowns, where the unknowns are the desired Fourier components and their complex conjugates. Although it may appear that knowledge of $\hat{D}_I(u_r,v,\theta;\phi_{in}^{(1)}=0)$ and $\hat{D}_I(u_r,v,\theta;\phi_{in}^{(2)}=\phi)$ is not sufficient for determination of $\hat{F}[u_r,v,\omega(u_r,v,\phi);\theta]$ and, hence, an estimate of $f(\vec{r})$, we will demonstrate that the use of tomographic symmetries will indeed make this possible.

B. Fourier space symmetries

In the development of our image reconstruction theory, it will prove useful to identify Fourier space symmetries that relate the Fourier components that appear in Eqs. (18) and (19). The functions $\hat{F}[u_r,v,\omega(u_r,v,0);\theta]$ and $\hat{F}[-u_r,-v,\omega(-u_r,-v,0);\theta]$ that appear in Eq. (18) describe Fourier components that reside on different halves of a spherical surface with radius k that is centered at $(0,0,-k)$ in the rotated coordinate system. This surface will be denoted as S_0. The functions $\hat{F}[u_r,v,\omega(u_r,v,\phi);\theta]$ and $\hat{F}[-u_r,-v,\omega(-u_r,-v,\phi);\theta]$ that appear in Eq. (19) describe Fourier components that reside on different halves of a spherical surface with radius k that is centered at $(-k\sin\phi,0,-k\cos\phi)$ in the rotated coordinate system. This surface will be denoted as S_ϕ. A simple but useful observation is that by rotating one of the surfaces about the v axis (the direction $\hat{s}_2$), S_0 and S_ϕ can be made to intersect at prescribed locations. Below, this observation is formulated mathematically.

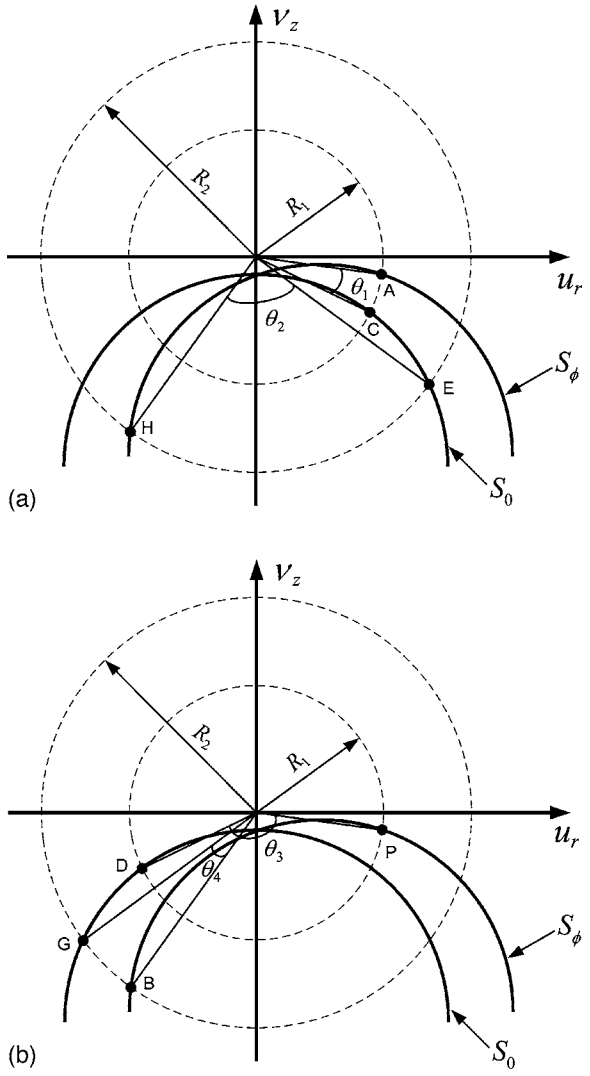

FIG. 4. Illustration of the symmetry properties described in Sec. III B. (a) The intersection of the semi-Ewald surfaces S_0 and S_ϕ with the plane of constant v. (b) The intersection of the semi-Ewald surfaces S_0 and S_ϕ with the plane of constant $-v$.

Let $\vec{K}_A=(u_r,v,\omega(u_r,v,\phi))$ and $\vec{K}_B=(-u_r,-v,\omega(-u_r,-v,\phi))$ denote the locations of the Fourier components $\hat{F}[u_r,v,\omega(u_r,v,\phi);\theta]$ and $\hat{F}[-u_r,-v,\omega(-u_r,-v,\phi);\theta]$, respectively. The locations of these components in planes of constant $\pm v$ that intersect S_ϕ are denoted by points A and B in Figs. 4(a) and 4(b), respectively. In each of these figures, the intersections of the surface S_0 with the same planes of constant $\pm v$ are displayed also. As shown in Fig. 4(a), let point C with location $\vec{K}_C=(u_1,v,\omega(u_1,v,0))$ denote a point on S_0 that is the same distance R_1 from the v axis as is point A that resides on S_ϕ. By use of elementary geometry, it can be verified that the value of the coordinate u_1 and radius R_1 must satisfy

$$u_1 = \mathrm{sgn}(u_r)\sqrt{R_1^2 - \frac{(R_1^2+v^2)^2}{4k^2}}, \tag{20}$$

where $\mathrm{sgn}(u_r)=1$ if $u_r \geqslant 0$ and $\mathrm{sgn}(u_r)=-1$ otherwise, and

$$R_1^2 = u_r^2 + (\sqrt{k^2-(u_r+k\sin\phi)^2-v^2}-k\cos\phi)^2. \tag{21}$$

Because $\vec{K}_A$ and $\vec{K}_C$ describe points on a circle that is concentric with the v axis, $\vec{K}_A$ can be made to coincide with $\vec{K}_C$ if S_ϕ is rotated by angle $-\theta_1$ about this axis. The angle θ_1 is given by

$$\theta_1 = \mathrm{atan}\left(\frac{u_1}{\sqrt{k^2-u_1^2-v^2}-k}\right) - \mathrm{atan}\left(\frac{u_r}{\sqrt{k^2-(u_r+k\sin\phi)^2-v^2}-k\cos\phi}\right) \tag{22}$$

and is indicated in Fig. 4(a). These observations establish the Fourier space symmetries

$$\hat{F}[u_1,v,\omega(u_1,v,0);\theta] = \hat{F}[u_r,v,\omega(u_r,v,\phi);\theta-\theta_1]. \tag{23}$$

In a similar way, let point G in Fig. 4(b) with location $\vec{K}_G=(-u_2,-v,\omega(-u_2,-v,0))$ reside on S_0 at the same distance R_2 from the v axis as is point B that resides on S_ϕ. It must be true that the value of the coordinate u_2 and radius R_2 satisfy

$$u_2 = \mathrm{sgn}(u_r)\sqrt{R_2^2 - \frac{(R_2^2+v^2)^2}{4k^2}} \tag{24}$$

and

$$R_2^2 = u_r^2 + (\sqrt{k^2-(u_r-k\sin\phi)^2-v^2}-k\cos\phi)^2. \tag{25}$$

Because $\vec{K}_B$ and $\vec{K}_G$ describe points on a circle that is concentric with the v axis, $\vec{K}_B$ can be made to coincide with $\vec{K}_G$ if S_ϕ is rotated by angle $-\theta_4$ about the v axis. It can be verified that θ_4 is given by

$$\theta_4 = -\mathrm{atan}\left(\frac{u_2}{\sqrt{k^2-u_2^2-v^2}-k}\right) + \mathrm{atan}\left(\frac{u_r}{\sqrt{k^2-(u_r-k\sin\phi)^2-v^2}-k\cos\phi}\right) \tag{26}$$

and is indicated in Fig. 4(b). We therefore obtain a second set of Fourier symmetries given by

$$\hat{F}[-u_2,-v,\omega(-u_2,-v,0);\theta] = \hat{F}[-u_r,-v,\omega(-u_r,-v,\phi);\theta-\theta_4]. \tag{27}$$

Applying the same logical steps as described above, a consideration of the relationship between points H and E in Fig. 4(a) and between points D and P in Fig. 4(b) yields two additional symmetry relations given by

$$\hat{F}[u_2,v,\omega(u_2,v,0);\theta] = \hat{F}[-u_r,v,\omega(-u_r,v,\phi);\theta+\theta_2] \tag{28}$$

and

$$\hat{F}[-u_1,-v,\omega(-u_1,-v,0);\theta] = \hat{F}[u_r,-v,\omega(u_r,-v,\phi);\theta-\theta_3], \tag{29}$$

where

$$\theta_2 = -\operatorname{atan}\left(\frac{u_2}{\sqrt{k^2-u_2^2-v^2}-k}\right) - \operatorname{atan}\left(\frac{u_r}{\sqrt{k^2-(u_r-k\sin\phi)^2-v^2}-k\cos\phi}\right) \quad (30)$$

and

$$\theta_3 = -\operatorname{atan}\left(\frac{u_1}{\sqrt{k^2-u_1^2-v^2}-k}\right) - \operatorname{atan}\left(\frac{u_r}{\sqrt{k^2-(u_r+k\sin\phi)^2-v^2}-k\cos\phi}\right). \quad (31)$$

The symmetries described by Eqs. (23) and (27)–(29) will be exploited in Sec. III C for the development of a tomographic reconstruction formula.

C. Reconstruction formula

Below we derive a novel reconstruction formula for off-axis holographic tomography. The general approach we adopt is to utilize the Fourier symmetries identified in Sec. III B, the rotational invariance of the problem, and Eqs. (18) and (19), to establish a linearly independent system of equations that can be solved to determine Fourier components of $f(\vec{r})$.

Consider Eq. (18) evaluated at frequencies (u_1,v),

$$\hat{D}_I(u_1,v,\theta;0) = a^+(u_1,v;0)\hat{F}[u_1,v,\omega(u_1,v,0);\theta] + a^-(u_1,v;0)\hat{F}^*[-u_1,-v,\omega(-u_1,-v,0);\theta], \quad (32)$$

and at frequencies (u_2,v),

$$\hat{D}_I(u_2,v,\theta;0) = a^+(u_2,v;0)\hat{F}[u_2,v,\omega(u_2,v,0);\theta] + a^-(u_2,v;0)\hat{F}^*[-u_2,-v,\omega(-u_2,-v,0);\theta]. \quad (33)$$

By use of the symmetry relations given in Eqs. (23) and (27)–(29), Eqs. (32) and (33) can be re-expressed as

$$\hat{D}_I(u_1,v,\theta;0) = a^+(u_1,v;0)\hat{F}[u_r,v,\omega(u_r,v,\phi);\theta-\theta_1] + a^-(u_1,v;0)\hat{F}^*[u_r,-v,\omega(u_r,-v,\phi);\theta-\theta_3] \quad (34)$$

and

$$\hat{D}_I(u_2,v,\theta;0) = a^+(u_2,v;0)\hat{F}[-u_r,v,\omega(-u_r,v,\phi);\theta+\theta_2] + a^-(u_2,v;0)\hat{F}^*[-u_r,-v,\omega(-u_r,-v,\phi);\theta-\theta_4]. \quad (35)$$

We will also consider Eq. (19) evaluated at frequencies $(-u_r,v)$:

$$\hat{D}_I(-u_r,v,\theta;\phi) = a^+(-u_r,v;\phi)\hat{F}[-u_r,v,\omega(-u_r,v,\phi);\theta] + a^-(-u_r,v;\phi)\hat{F}^*[u_r,-v,\omega(u_r,-v,\phi);\theta]. \quad (36)$$

Equations (19) and (34)–(36) form a system of *four* equations with *eight* unknowns. The unknowns represent the sought after Fourier components of $f(\vec{r})$ and their complex conjugates. We will now utilize these equations and the rotational invariance of the problem to establish a linearly independent 4×4 system that can be solved uniquely.

Because $\hat{D}_I(u_r,v,\theta;0)$ and $\hat{D}_I(u_r,v,\theta;\phi)$ are 2π-periodic functions of θ, they can be expressed by their Fourier series as

$$\hat{D}_I(u_r,v,\theta;0) = \sum_{n=-\infty}^{\infty} D_{0,n}(u_r,v)\exp[in\theta] \quad (37)$$

and

$$\hat{D}_I(u_r,v,\theta;\phi) = \sum_{n=-\infty}^{\infty} D_{\phi,n}(u_r,v)\exp[in\theta], \quad (38)$$

where

$$D_{0,n}(u_r,v) = \frac{1}{2\pi}\int_0^{2\pi} \hat{D}_I(u_r,v,\theta;0)\exp[-in\theta]\,d\theta \quad (39)$$

and

$$D_{\phi,n}(u_r,v) = \frac{1}{2\pi}\int_0^{2\pi} \hat{D}_I(u_r,v,\theta;\phi)\exp[-in\theta]\,d\theta. \quad (40)$$

By use of Eqs. (39) and (40), one finds readily from Eqs. (19) and (34)–(36) that

$$D_{0,n}(u_1,v) = a^+(u_1,v;0)\hat{F}_n(u_r,v)\exp[-in\theta_1] + a^-(u_1,v;0)\hat{F}^*_{-n}(u_r,-v)\exp[-in\theta_3], \quad (41)$$

$$D_{0,n}(u_2,v) = a^+(u_2,v;0)\hat{F}_n(-u_r,v)\exp[in\theta_2] + a^-(u_2,v;0) \times \hat{F}^*_{-n}(-u_r,-v)\exp[-in\theta_4], \quad (42)$$

$$D_{\phi,n}(u_r,v) = a^+(u_r,v;\phi)\hat{F}_n(u_r,v) + a^-(u_r,v;\phi)\hat{F}^*_{-n}(-u_r,-v), \quad (43)$$

and

$$D_{\phi,n}(-u_r,v) = a^+(-u_r,v;\phi)\hat{F}_n(-u_r,v) + a^-(-u_r,v;\phi) \times \hat{F}^*_{-n}(u_r,-v). \quad (44)$$

The quantity

$$\hat{F}_n(u_r,v)=\frac{1}{2\pi}\int_0^{2\pi}\hat{F}[u_r,v,\omega(u_r,v,\phi);\theta]\exp[-in\theta]\,d\theta \tag{45}$$

describes the Fourier series expansion coefficients of $\hat{F}[u_r,v,\omega(u_r,v,\phi);\theta]$, which is a 2π-periodic function of θ.

Equations (41)–(44) represent a linearly independent system of *four* equations with *four* unknowns, where the unknowns represent the expansion coefficients (and their conjugates) of the desired Fourier components of $f(\vec{r})$. The solution of this system yields

$$\hat{F}_n(u_r,v)=\frac{1}{M}\begin{vmatrix} D_{0,n}(u_1,v) & 0 & a^-(u_1,v;0)e^{-in\theta_3} & 0 \\ D_{0,n}(u_2,v) & a^+(u_2,v;0)e^{in\theta_2} & 0 & a^-(u_2,v;0)e^{-in\theta_4} \\ D_{\phi,n}(u_r,v) & 0 & 0 & a^-(u_r,v;\phi) \\ D_{\phi,n}(-u_r,v) & a^+(-u_r,v;\phi) & a^-(-u_r,v;\phi) & 0 \end{vmatrix}, \tag{46}$$

where

$$M=\begin{vmatrix} a^+(u_1,v;0)e^{-in\theta_1} & 0 & a^-(u_1,v;0)e^{-in\theta_3} & 0 \\ 0 & a^+(u_2,v;0)e^{in\theta_2} & 0 & a^-(u_2,v;0)e^{-in\theta_4} \\ a^+(u_r,v;\phi) & 0 & 0 & a^-(u_r,v;\phi) \\ 0 & a^+(-u_r,v;\phi) & a^-(-u_r,v;\phi) & 0 \end{vmatrix}, \tag{47}$$

and the spatial frequencies u_r and v satisfy the conditions given in Eqs. (14).

Equation (46), which is the key result of this paper, permits determination of the Fourier data $\hat{F}[u_r,v,\omega(u_r,v,\phi);\theta]$ as

$$\hat{F}[u_r,v,\omega(u_r,v,\phi);\theta]=\sum_{n=-\infty}^{\infty}\hat{F}_n(u_r,v)\exp[in\theta]. \tag{48}$$

From knowledge of $\hat{F}[u_r,v,\omega(u_r,v,\phi);\theta]$, an estimate of $f(\vec{r})$ can be reconstructed by use of a DT reconstruction algorithm [8]. In the appendix, we develop a novel DT reconstruction algorithm [28,29] that will be employed in our numerical studies.

D. Features of the reconstruction formula

For a given illumination angle $\phi_{in}^{(2)}=\phi$, the determinant M defined in Eq. (47) can take on zero values at certain frequencies (u_r,v). Consequently, the expression for the expansion coefficients $\hat{F}_n(u_r,v)$ contains isolated poles at these frequencies. Although this poses no mathematical difficulties, as discussed in Sec. IV, an explicit consideration of the poles must be taken when implementing the formula numerically. The values of $\hat{F}_n(u_r,v)$ corresponding to (u_r,v) near a singularity can be significantly corrupted due to amplification of noise and other inconsistencies in the measurement data. The locations of the poles in Eq. (46) depend, in a nontrivial way, on the value of the wave number k and second illumination angle $\phi_{in}^{(2)}=\phi$. (Recall that, as described in Sec. III A, the illumination angle for the first measurement is fixed at $\phi_{in}^{(1)}=0$.) It can be verified readily that one such pole in Eq. (46) exists at $u_r=v=0$. This indicates that, as in I-DT using a conventional in-line geometry [15,16], it can be difficult to reconstruct accurately certain low-frequency components of $f(\vec{r})$ from noisy measurement data. In practice, regularization methods should be employed to mitigate the effects of poles in the reconstruction formula. A numerical demonstration of this is provided in Sec. IV.

The value of the illumination angle $\phi_{in}^{(2)}$ also determines the achievable spatial resolution of the imaging method. As mentioned previously, in this work, we assume that evanescent wave modes do not contribute significantly to the measurement data. In practice, this will be the case unless the detector plane is placed sufficiently close [30] to the object.

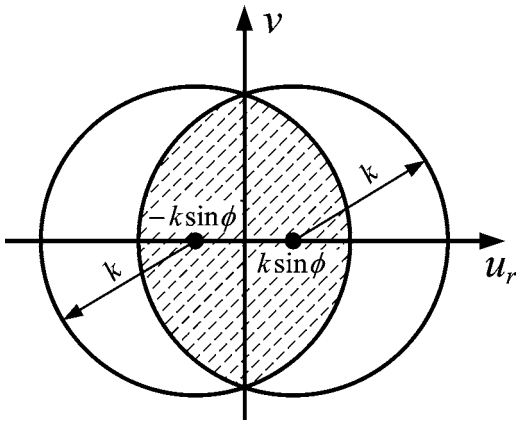

FIG. 5. The shaded region denotes the collection of spatial frequencies (u_r,v) that satisfy $k^2>(u_r\pm k\sin\phi)^2+v^2$. See Sec. III D for a complete description.

With consideration of propagating wave modes only, the spatial frequencies (u_r, v) in Eq. (46) are restricted to satisfy the conditions in Eq. (14). These conditions, shown graphically in Fig. 5, require that (u_r, v) specify locations that reside within the intersection of two circles of radius k with centers $u_r = \pm k \sin \phi_{in}^{(2)}$ in the u_r-v plane, where $\phi_{in}^{(2)} \in (-\pi/2, \pi/2)$ and $\phi_{in}^{(2)} \neq 0$. The area of overlap of these circles monotonically increases as $\phi_{in}^{(2)}$ decreases; this indicates that more spatial frequencies of $f(\vec{r})$ can be determined as $\phi_{in}^{(2)}$ decreases. However, the reconstruction formula in Eq. (46) becomes singular as $\phi_{in}^{(2)} \to 0$, and therefore, use of a sufficiently small illuminating angle $\phi_{in}^{(2)}$ will cause instabilities in the numerical reconstructions. This indicates a tradeoff between spatial resolution and stability. It should be noted that due to other poles in Eq. (46) away from the origin, the global nature of this tradeoff is not transparent.

E. Alternative symmetries and reconstruction formulae

Alternative Fourier space symmetries to the ones presented in Sec. III B can be identified. For example, it can be verified that

$$\hat{F}[u_1', v, \omega(u_1', v, 0); \theta] = \hat{F}[u_r, v, \omega(u_r, v, \phi); \theta - \theta_1'], \quad (49)$$

$$\hat{F}^*[-u_1', -v, \omega(-u_1', -v, 0); \theta] = \hat{F}^*[u_r, -v, \omega(u_r, -v, \phi); \theta - \theta_3'], \quad (50)$$

where

$$u_1' = \mathrm{sgn}(-u_r) \sqrt{R_1^2 - \frac{(R_1^2 + v^2)^2}{4k^2}}, \quad (51)$$

$$\theta_1' = -\mathrm{atan}\left(\frac{u_1'}{\sqrt{k^2 - u_1'^2 - v^2} - k} \right) - \mathrm{atan}\left(\frac{u_r}{\sqrt{k^2 - (u_r + k \sin \phi)^2 - v^2} - k \cos \phi} \right), \quad (52)$$

and

$$\theta_3' = \mathrm{atan}\left(\frac{u_1'}{\sqrt{k^2 - u_1'^2 - v^2} - k} \right) - \mathrm{atan}\left(\frac{u_r}{\sqrt{k^2 - (u_r + k \sin \phi)^2 - v^2} - k \cos \phi} \right). \quad (53)$$

By use of these symmetries, following the same general procedure as described in Sec. III C, one can derive an alternative reconstruction formula that is mathematically equivalent to Eq. (46). However, the locations of its singularities and, hence, the numerical properties of the resulting reconstruction algorithm will differ. In fact, it may be possible to identify several other Fourier space symmetry properties that can be utilized for the development of a class of reconstruction formulae. We leave the development and exploration of these alternative reconstruction formulae as topics for future investigation.

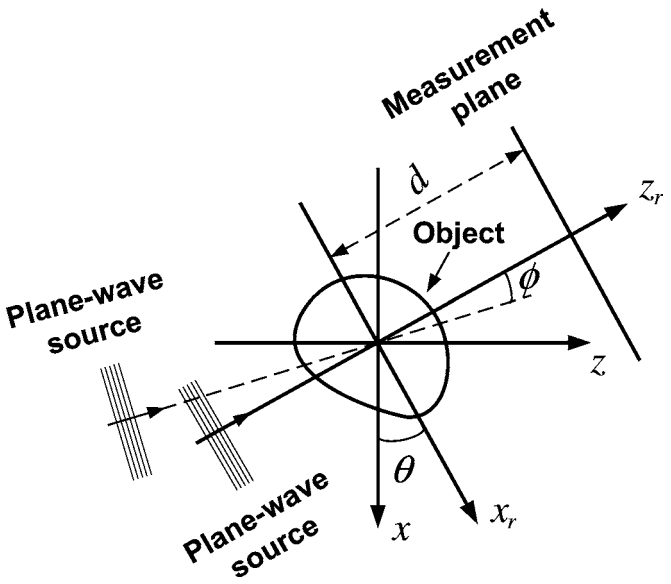

FIG. 6. The 2D scanning geometry utilized in the computer-simulation studies.

IV. NUMERICAL RESULTS

Computer-simulation studies were conducted to validate and demonstrate the reconstruction method described in Sec. III. Although the reconstruction theory can accommodate 3D objects, in this preliminary numerical study, a 2D object is assumed.

A. Phantom and simulation data

The 2D mathematical phantom shown in Fig. 7 was taken to represent the complex-valued refractive index distribution of the object. Horizontal profiles through the phantom are superimposed on the reconstructed profiles that are described later. The length of the long and the short axes of the largest ellipse (i.e., the background structure) was 0.9 mm and 0.7 mm, respectively. Our simulations assumed that we employed the 2D off-axis holographic scanning geometry depicted in Fig. 6. A plane wave with wavelength $\lambda = 0.5 \times 10^{-5}$ m illuminates the object at incident angles $\phi_{in}^{(1)} = 0$ and $\phi_{in}^{(2)} = -\pi/8$. In each case, the intensity of the transmitted wavefield is measured on a detector array located at distance 4 mm behind from the scatterer. The detector array has a length of 1.024 cm and contains 1024 elements (therefore, the detector sampling interval is $\Delta x_r = 1 \times 10^{-5}$ m).

The intensity data $I(x_r, \theta; 0)$ and $I(x_r, \theta; -\pi/8)$ were calculated by use of Eqs. (18) and (19), respectively, along with Eq. (10). Here and elsewhere, the v and y dependencies of the equations were omitted. Because the phantom was composed of ellipses, the necessary Fourier data that appear in Eqs. (18) and (19) was calculated analytically. Generation of the simulation data in this way presumes the validity of the first-Rytov weak scattering condition. The deleterious effects of strong scattering are not addressed by the reconstruction theory, which is predicated upon weak scattering conditions. $I(x_r, \theta; 0)$ and $I(x_r, \theta; -\pi/8)$ were calculated at 360 tomographic view angles θ that were evenly sampled over $[0, 2\pi)$.

To model the effects of measurement noise and other data inconsistencies, the intensity data were treated as realizations of an uncorrelated Gaussian random process with mean μ and standard deviation σ. In our simulation, $\mu=\mu(x_r,\theta)$ was set equal to the noiseless value of the wavefield intensity and σ was chosen to satisfy $\sigma/\mu=0.1\%$ and 0.2%.

B. Reconstruction procedure

The intensity data functions $D_I(x_r,\theta;\phi_{in}^{(1)}=0)$ and $D_I(x_r,\theta;\phi_{in}^{(2)}=-\pi/8)$ were computed from the simulated noiseless and noisy intensity data by use of Eq. (10). The one-dimensional (1D) fast Fourier transform (FFT) algorithm was applied subsequently for computation of $\hat{D}_I(u_r,\theta;0)$ and $\hat{D}_I(u_r,\theta;-\pi/8)$ at uniformly spaced values of u_r. To compute the nonuniformly spaced Fourier data $\hat{D}_I(u_1,\theta;0)$ and $\hat{D}_I(u_2,\theta;0)$, a 1D interpolation was utilized. Prior to the interpolation, the sampling density of the uniformly sampled Fourier data $\hat{D}_I(u_r,\theta;0)$ was increased by a factor of 16 by use of zero-padding interpolation [31]. The expansion coefficients $D_{0,n}(u_1)$, $D_{0,n}(u_2)$, $D_{0,\phi}(u_r)$, and $D_{0,\phi}(-u_r)$ were computed by applying the FFT algorithm to the sampled angular coordinate θ of the data functions $\hat{D}_I(u_1,\theta;0)$, $\hat{D}_I(u_2,\theta;0)$, $\hat{D}_I(u_r,\theta;-\pi/8)$, and $\hat{D}_I(-u_r,\theta;-\pi/8)$, respectively. From knowledge of these quantities, Eq. (46) was utilized to determine $\hat{F}_n(u_r)$ at frequencies u_r that satisfied

$$k^2 > (u_r \pm k \sin\phi_{in}^{(2)})^2, \tag{54}$$

where $\phi_{in}^{(2)}=-\pi/8$. For reconstruction from the noisy data sets, a simple thresholding strategy was employed to mitigate the effects of the singularities in Eq. (46). Specifically, Eq. (46) was employed to determine $\hat{F}_n(u_r)$ only for frequencies that satisfied $M>\epsilon$, where ϵ was a preset threshold value. In this work, the value of ϵ was set at 0.0025. For frequencies that did not satisfy this condition, i.e., at or near the locations of singularities in Eq. (46), the value of $\hat{F}_n(u_r)$ was set to zero. Finally, $\hat{F}[u_r,\omega(u_r,\phi_{in}^{(2)});\theta]$ was calculated by use of Eq. (48) and an estimate of $f(\vec{r})$ was obtained by use of the DT reconstruction algorithm derived in the appendix. The complex-valued refractive index distribution $n(\vec{r})$ was determined from $f(\vec{r})$ by use of Eq. (2). The matrix size of the reconstructed images was 120×120 pixels.

C. Reconstructed images

Figure 8 displays images of $n(\vec{r})$ reconstructed from the noiseless simulation data. The real and imaginary components are contained in Figs. 8(a) and 8(b), respectively. Profiles through the central rows of Figs. 8(a) and 8(b) are represented by the dashed lines in Fig. 9(a) and 9(b), respectively. In both figures, the profiles corresponding to the true object are represented by a solid line. These results confirm that our reconstruction method can reconstruct accurate estimates of $n(\vec{r})$ [or, equivalently, $f(\vec{r})$] from consistent measurement data.

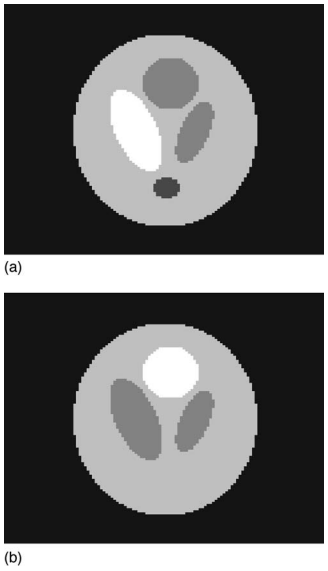

FIG. 7. A 2D mathematical phantom that is used in the simulation studies. (a) and (b) display the real and imaginary components of the phantom, respectively.

Figures 10 and 12 contain images of $n(\vec{r})$ reconstructed from the noisy simulation data corresponding to noise levels $\sigma/\mu=0.1\%$ and $\sigma/\mu=0.2\%$, respectively. In each case, the real and imaginary components are displayed in subfigures (a) and (b), respectively. Profiles through the central rows of Figs. 10(a) and 10(b) are represented by the dashed lines in the corresponding plots in Fig. 11. Similarly, the profiles through the central rows of Figs. 12(a) and 12(b) are represented by the dashed lines in the corresponding plots in Fig. 13. In both cases, the profiles corresponding to the true object are displayed as solid lines. These results confirm that it is possible to reconstruct reasonable images from noise-contaminated measurement data. For the noise level considered, it was found that the regularization method based on a

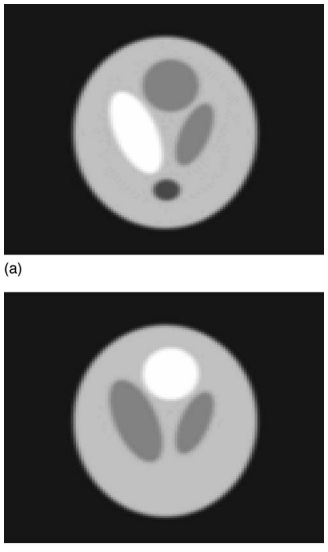

FIG. 8. Images of (a) $\mathrm{Re}\{n(\vec{r})\}-1$ and (b) $\mathrm{Im}\{n(\vec{r})\}$ reconstructed from the noiseless simulation data.

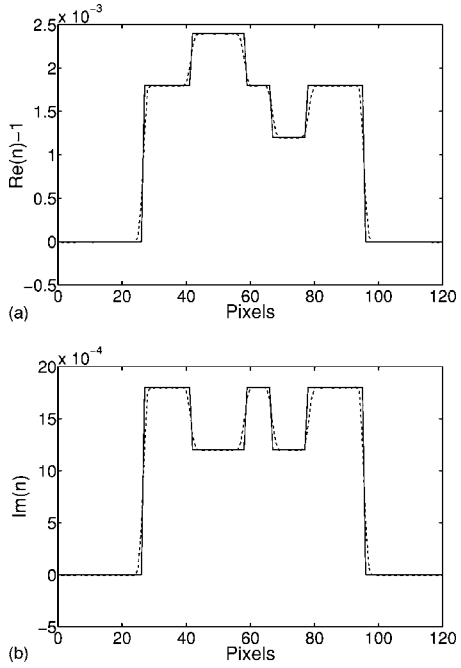

FIG. 9. (a) Profiles through the central rows of Figs. 7(a) and 8(a) are represented by solid and dashed curves, respectively. (b) Profiles through the central rows of Figs. 7(b) and 8(b) are represented by solid and dashed curves, respectively.

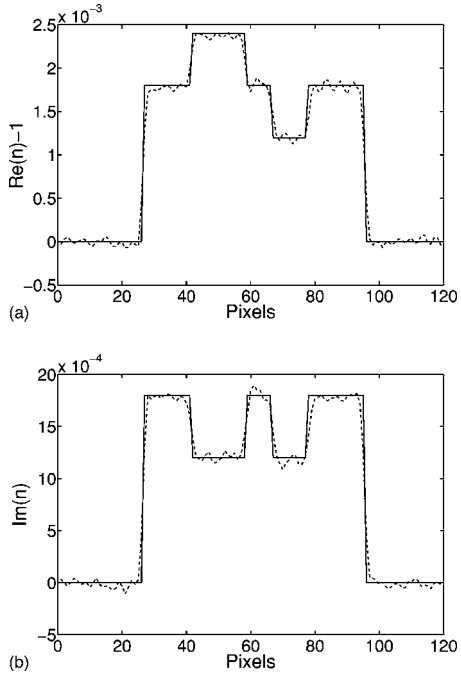

FIG. 11. (a) Profiles through the central rows of Figs. 7(a) and 10(a) are represented by solid and dashed curves, respectively. (b) Profiles through the central rows of Figs. 7(b) and 10(b) are represented by solid and dashed curves, respectively.

simple thresholding of the Fourier expansion coefficients was effective enough to avoid a large noise amplification in the reconstructed images (see Fig. 12). For higher noise levels, more sophisticated regularization methods [32,33] may be warranted.

V. SUMMARY

Diffraction tomography is a well-studied imaging method that permits reconstruction of the 3D complex-valued refractive index distribution of weakly scattering objects. The success of DT imaging in optical applications has been limited because it requires explicit knowledge of the phase of the transmitted wavefields, which can pose well-known experimental difficulties. A theory of intensity DT has been proposed that circumvents the phase-retrieval problem by replacing explicit phase measurements on a single detector plane by intensity measurements on two or more different parallel planes. Each of these intensity measurements repre-

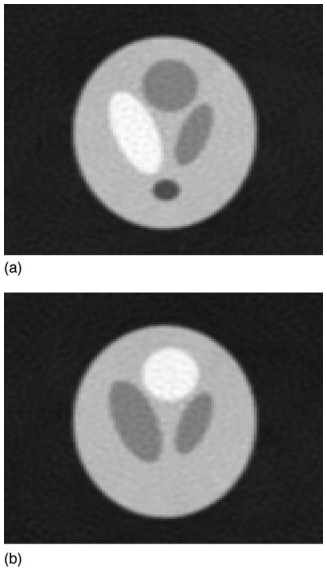

FIG. 10. Images of (a) $\mathrm{Re}\{n(\vec{r})\}-1$ and (b) $\mathrm{Im}\{n(\vec{r})\}$ reconstructed from the noisy simulation data with noise level 0.1%.

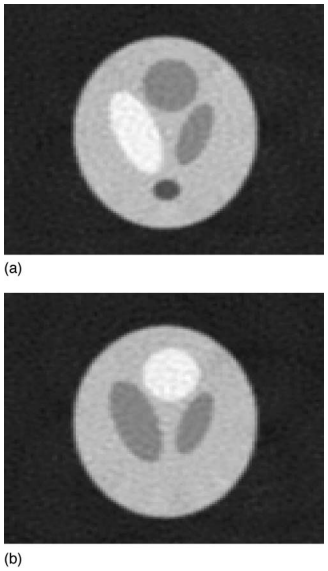

FIG. 12. Images of (a) $\mathrm{Re}\{n(\vec{r})\}-1$ and (b) $\mathrm{Im}\{n(\vec{r})\}$ reconstructed from the noisy simulation data with noise level 0.2%.

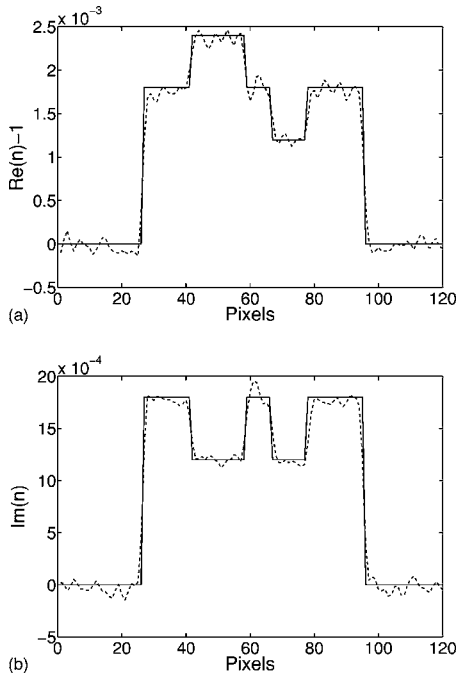

FIG. 13. (a) Profiles through the central rows of Figs. 7(a) and 12(a) are represented by solid and dashed curves, respectively. (b) Profiles through the central rows of Figs. 7(b) and 12(b) are represented by solid and dashed curves, respectively.

sents an in-line hologram, in which information regarding the wavefield phase is encoded as variations in the recorded intensity. From knowledge of these intensity measurements acquired at a collection of tomographic view angles, an estimate of the object's 3D complex-valued refractive index distribution can be reconstructed.

In this work, a reconstruction theory for *off-axis* holographic tomography with diffracting scalar wavefields was developed and investigated. Off-axis holographic tomography is a generalized in-line I-DT method, but differs from conventional I-DT in that two intensity measurements are acquired on a single *fixed* detector plane behind the object. The first of these measurements corresponds to an illuminating plane wave propagating in a direction that is perpendicular to the detector plane. This measurement is the same as would be acquired in a conventional in-line I-DT geometry. However, the second measurement corresponds to an illuminating plane wave propagating obliquely with respect to this direction. Accordingly, in off-axis holographic tomography, the direction of the incident plane wave represents the degree of freedom that is varied for acquisition of the measurement data rather than the detector location as in conventional in-line methods. This measurement strategy may have significant benefits in a wide range of imaging studies [5,27,34,35]. For example, because at each tomographic view angle the detector location remains fixed, there is no need to spatially register two intensity measurements as is required by conventional in-line methods. An assessment of the practical advantages of the off-axis measurement geometry for specific applications remains an interesting topic for future investigation.

Our method differs from classic sideband holographic approaches [11,22] in that it does not involve the use of an unperturbed reference beam to illuminate the recorded hologram. Both intensity measurements at each tomographic view angle correspond to wavefields that illuminate the object. Additionally, it permits direct reconstruction of the refractive index distribution without an explicit intermediate step of recovering the wavefield phase. Unlike phase-retrieval methods based on the transport of intensity equation [12,36], our reconstruction method is I-DT based and, therefore, does not require a paraxial assumption to describe the transmitted wavefield.

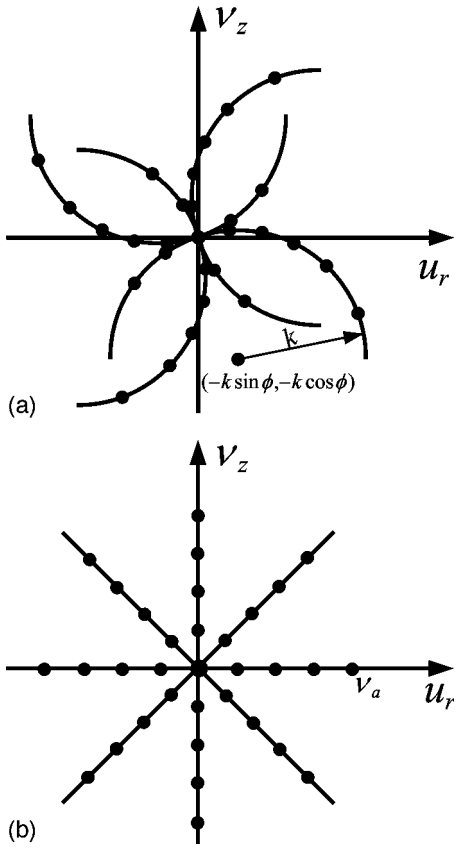

FIG. 14. (a) Fourier data evaluated on unevenly sampled semi-arcs. (b) Fourier data evaluated on a uniform polar grid.

The derivations of the tomographic reconstruction formulae were facilitated by exploiting certain Fourier space symmetries, which are a consequence of the wave propagation physics and the rotational invariance of the tomographic imaging model. A similar solution strategy was employed in our recent study of spherical wave I-DT [37]. The choice of the illuminating angle of the probing plane wave was found to affect the inherent stability and resolution properties of the reconstruction method. A preliminary computer-simulation study was conducted to validate the method. A comprehensive investigation of the numerical and statistical properties of the reconstruction method is an important topic for future study.

APPENDIX

In this appendix, we derive a novel 2D DT reconstruction algorithm that was employed in our numerical simulations.

The extension to the full 3D case follows readily. Mathematically, an estimate of $f(\vec{r})$ can be obtained from the determined $\hat{F}[u_r, \omega(u_r, \phi); \theta]$ via an inverse Fourier transformation. The algorithm described below can perform this reconstruction from knowledge of the nonuniformly spaced samples of $\hat{F}[u_r, \omega(u_r, \phi); \theta]$ that are determined in practice. The basic idea is to convert the collection of nonuniformly sampled Fourier data residing on semicircles to a collection of samples that reside on a uniform polar grid. Subsequently, the filtered backprojection (FBP) algorithm [31] of conventional x-ray computerized tomography (CT) can be employed for efficient and robust image reconstruction. This solution strategy, which was first proposed by Pan [28], has proven effective in related DT reconstruction problems [29,38].

Let $\hat{F}(\nu_a; \theta)$ denote the 2D Fourier transform of $f(\vec{r})$ expressed in polar coordinates that is defined as

$$\hat{F}(\nu_a; \theta) = \int_{-\infty}^{\infty} \int_{-\infty}^{\infty} f(x,y) e^{-i\nu_a(x \cos \theta + y \sin \theta)} dx dy. \quad \text{(A1)}$$

Consider $\hat{F}[u_r, \omega(u_r, \phi); \theta]$ evaluated at the frequencies ν_1 and ν_2, respectively, where

$$\nu_1 = \frac{\nu_a(\sqrt{4k^2 - \nu_a^2} \cos \phi - \nu_a \sin \phi)}{2k} \quad \text{(A2)}$$

and

$$\nu_2 = \frac{-\nu_a(\sqrt{4k^2 - \nu_a^2} \cos \phi + \nu_a \sin \phi)}{2k}. \quad \text{(A3)}$$

It can be verified that

$$\hat{F}(\nu_a; \theta) = \hat{F}[\nu_1, \omega(\nu_1, \phi); \theta + \theta_1'] \quad \text{(A4)}$$

and

$$\hat{F}(\nu_a; \theta) = \hat{F}[\nu_2, \omega(\nu_2, \phi); \theta + \theta_2'], \quad \text{(A5)}$$

where

$$\theta_1' = -\operatorname{atan}\left(\frac{\sqrt{k^2 - (\nu_1 + k \sin \phi)^2} - k \cos \phi}{\nu_1} \right) \quad \text{(A6)}$$

and

$$\theta_2' = \pi + \operatorname{atan}\left(\frac{\sqrt{k^2 - (\nu_2 + k \sin \phi)^2} - k \cos \phi}{\nu_2} \right). \quad \text{(A7)}$$

For simplicity, we only consider frequencies ν_a that simultaneously satisfy $k^2 > (\nu_1 + k \sin \phi)^2$ and $k^2 > (\nu_2 + k \sin \phi)^2$.

Because $\hat{F}[u_r, \omega(u_r, \phi); \theta]$ and $\hat{F}(\nu_a; \theta)$ are 2π-periodic functions of θ, they can be expressed by their Fourier series as

$$\hat{F}[u_r, \omega(u_r, \phi); \theta] = \sum_{n=-\infty}^{\infty} \hat{F}_n(u_r) e^{in\theta} \quad \text{(A8)}$$

and

$$\hat{F}(\nu_a; \theta) = \sum_{n=-\infty}^{\infty} \hat{P}_n(\nu_a) e^{in\theta}, \quad \text{(A9)}$$

where

$$\hat{F}_n(u_r) = \frac{1}{2\pi} \int_0^{2\pi} \hat{F}[u_r, \omega(u_r, \phi); \theta] e^{-in\theta} d\theta \quad \text{(A10)}$$

and

$$\hat{P}_n(\nu_a) = \frac{1}{2\pi} \int_0^{2\pi} \hat{F}(\nu_a; \theta) e^{-in\theta} d\theta. \quad \text{(A11)}$$

Substitution from Eqs. (A8) and (A9) into Eqs. (A4) and (A5) yields two estimations of $\hat{P}_n(\nu_a)$, namely,

$$\hat{P}_n(\nu_a) = \hat{F}_n(u_1) e^{in\theta_1'} \quad \text{(A12)}$$

and

$$\hat{P}_n(\nu_a) = \hat{F}_n(u_2) e^{in\theta_2'}. \quad \text{(A13)}$$

One can introduce a combination coefficient α to combine these two estimations [28,38] as

$$\hat{P}_n(\nu_a) = \alpha \hat{F}_n(u_1) e^{in\theta_1'} + (1 - \alpha) \hat{F}_n(u_2) e^{in\theta_2'}. \quad \text{(A14)}$$

In our simulations, the value $\alpha = \frac{1}{2}$ was employed. Equations (A14) and (A9) permit determination of the Fourier data $\hat{F}(\nu_a; \theta)$ residing on a uniform polar grid. The final reconstruction of $f(\vec{r})$ can be obtained subsequently by application of the FBP algorithm.

[1] E. Wolf, Opt. Commun. **1**, 153 (1969).
[2] E. Wolf, in *Trends in Optics*, edited by A. Consortini (Academic, San Diego, 1996), pp. 83–110.
[3] A. J. Devaney, in *Inverse Methods in Electromagnetic Imaging, Part 2*, edited by W. M. Boerner, NATO ASI Series (Plenum, New York, 1983), pp. 1107–1135.
[4] T. Wedberg and J. Stamnes, Opt. Rev. **2**, 28 (1995).
[5] V. Lauer, J. Microsc. **205**, 165 (2001).
[6] P. S. Carney and J. C. Schotland, Appl. Phys. Lett. **77**, 2798 (2000).
[7] T. Beetz, C. Jacobsen, and A. Stein, J. Phys. IV **104**, 31 (2003).
[8] A. J. Devaney, IEEE Trans. Geosci. Remote Sens. **GE–22**, 3 (1984).
[9] P. Grassin, B. Duchene, and W. Tabbara, in *Mathematical Methods in Tomography*, (Springer-Verlag, Heidelberg, 1991), pp. 98–105.
[10] T. Mast, J. Acoust. Soc. Am. **106**, 3061 (1999).
[11] E. N. Leith and J. Upatnieks, J. Opt. Soc. Am. **53**, 1377 (1963).

[12] K. A. Nugent, T. E. Gureyev, D. Cookson, D. Paganin, and Z. Barnea, Phys. Rev. Lett. **77**, 2961 (1996).
[13] M. Maleki and A. Devaney, J. Opt. Soc. Am. A **10**, pp. 1086–1092 (1993).
[14] A. J. Devaney, IEEE Trans. Image Process. **1**, 221 (1992).
[15] G. Gbur and E. Wolf, J. Opt. Soc. Am. A **19**, 2194 (2002).
[16] G. Gbur and E. Wolf, Opt. Lett. **27**, 1890 (2002).
[17] J. Cheng and S. Han, J. Opt. Soc. Am. A **18**, 1460 (2001).
[18] D. Shi, M. A. Anastasio, Y. Huang, and G. Gbur, Phys. Med. Biol. **49**, 2733 (2004).
[19] G. Gbur, M. A. Anastasio, Y. Huang, and D. Shi, J. Opt. Soc. Am. A **22**, 230 (2005).
[20] D. Gabor, Nature (London) **161**, 777 (1948).
[21] M. Born and E. Wolf, *Principles of Optics*, 7th ed. (Cambridge University Press, Cambridge, UK, 1999).
[22] E. Wolf, J. Opt. Soc. Am. **60**, 18 (1970).
[23] B. Chen and J. J. Stamnes, Appl. Opt. **37**, 2996 (1998).
[24] M. A. Anastasio and D. Shi, in *Physics of Medical Imaging, Progress in Biomedical Optics and Imaging*, Proceedings of the SPIE, (SPIE, Bellingham, WA, 2005) Vol. 5745, pp. 1266–1271.
[25] Z. Lu, Inverse Probl. **1**, 339 (1985).
[26] M. A. Anastasio, PhD thesis, The University of Chicago, 2001.
[27] S. Mayo, T. Davis, T. Gureyev, P. Miller, D. Paganin, A. Pogany, A. Stevenson, and S. Wilkins, Opt. Express **11**, 2289 (2003).
[28] X. Pan, J. Opt. Soc. Am. A **15**, 2312 (1998).
[29] M. A. Anastasio and X. Pan, J. Opt. Soc. Am. A **17**, 391 (2000).
[30] R. A. Frazin, D. G. Fischer, and P. S. Carney, J. Opt. Soc. Am. A **21**, 1050 (2004).
[31] A. Kak and M. Slaney, *Principles of Computerized Tomographic Imaging* (IEEE Press, New York, 1988).
[32] M. Bertero and P. Boccacci, *Introduction to Inverse Problems in Imaging* (Institute of Physics, Bristol, 1998).
[33] R. Bernier and H. H. Arsenault, Appl. Opt. **30**, 5163 (1991).
[34] A. Barty, K. A. Nugent, A. Roberts, and D. Paganin, Opt. Commun. **175**, 329 (2000).
[35] P. Spanne, C. Raven, I. Snigireva, and A. Snigirev, Phys. Med. Biol. **44**, 741 (1999).
[36] M. R. Teague, J. Opt. Soc. Am. **73**, 1434 (1983).
[37] M. A. Anastasio, D. Shi, Y. Huang, and G. Gbur, Journal of the Optical Society of America (to be published).
[38] M. A. Anastasio and X. Pan, Int. J. Imaging Syst. Technol. **10**, 437 (1999).